Hybrid simulations of chromospheric HXR flare sources

Z. Moravec[1,⋆], **M. Varady**[1,2], **J. Kašparová**[2], and **D. Kramoliš**[1]

[1] J. E. Purkyně University, Faculty of Science, České mládeže 8, CZ-400 96 Ústí nad Labem, Czech Republic
[2] Astronomical Institute of the CAS, Fričova 298, 25165 Ondřejov, Czech Republic

Received 14 Dec 2015, accepted ?????
Published online later

Key words Sun: flares – chromosphere – X-rays

Recent measurements of vertical extents and positions of the chromospheric hard X-ray (HXR) flare sources based on Ramaty High-Energy Spectroscopic Imager (RHESSI) observations show a significant inconsistency with the theoretical predictions based on the standard collisional thick target model (CTTM). Using a hybrid flare code Flarix, we model simultaneously and self-consistently the propagation, scattering and energy losses of electron beams with power-law energy spectra and various initial pitch-angle distributions in a purely collisional approximation and concurrently the dynamic response of the heated chromosphere on timescales typical for RHESSI image reconstruction. The results of the simulations are used to model the time evolution of the vertical distribution of chromospheric HXR source within a singular (compact) loop. Adopting the typical RHESSI imaging times scales, energy dependent vertical sizes and positions as could be observed by RHESSI are presented.

© 2016 WILEY-VCH Verlag GmbH & Co. KGaA, Weinheim

arXiv:1601.07026v1 [astro-ph.SR] 26 Jan 2016

1 Introduction

RHESSI (Lin et al. 2002) observations of chromospheric HXR sources in solar flares present an invaluable diagnostics on the properties of high energy electrons involved in the non-thermal bremsstrahlung emission process in the thick target region and on the properties of the target chromospheric plasma (Brown 1971), providing thus an excellent basis for testing of theoretical predictions of flare models.

The novel measurements of vertical sizes and positions of chromospheric HXR sources in flares (e.g. Battaglia & Kontar 2011; Krucker et al. 2015; Martínez Oliveros et al. 2012) based on the RHESSI imaging ability (Hurford et al. 2002; Lin et al. 2002) are one of such tests. The source sizes in the direction of the magnetic field measured by Battaglia & Kontar (2011) are in the range from 1.3 arcsec up to 8 arcsec and hereby inconsistent with the predictions given by the standard CTTM (Brown 1971). The theoretical source sizes obtained for static VAL C atmosphere (Vernazza et al. 1981) without magnetic mirroring in the CTTM approximation are energy dependent, but always smaller than the lower values obtained from observations, for high energies even being sub-arcsecond (e.g. Moravec et al. 2013; Varady et al. 2013). The HXR source positions for two studied footpoint sources according to Martínez Oliveros et al. (2012) are surprisingly close to the photosphere with heights from 200 km to 400 km and uncertainty $\pm$200 km, thus ruling out the CTTM. Krucker et al. (2015) obtained substantially higher positions for three flares, ranging from 600 km to 1050 km including uncertainties. The upper values of these measurements are at the lower limit predicted by CTTM. Their lower values, and especially those obtained by Martínez Oliveros et al. (2012), rule out the standard CTTM and imply a necessity of alternative models (Fletcher & Hudson 2008) or modifications of the CTTM, e.g. by introducing a re-acceleration of non-thermal electrons in the chromosphere (Brown et al. 2009; Turkmani et al. 2006; Varady et al. 2014).

There have been several attempts to explain the inconsistency between the theoretical and observed vertical extents of the chromospheric HXR sources. Battaglia et al. (2012) modelled the vertical sizes of the HXR sources for several prescribed density distributions along the loop, for various pitch-angle distributions in a singular (compact) flare loop with converging magnetic field (i.e. including magnetic mirroring). They obtained theoretical source sizes smaller than 1.5 arcsec, thus inconsistent with the observed values. Another attempt (O'Flannagain et al. 2015) attributes the discrepancy to the presence of neutral hydrogen in the chromospheric thick target region. The authors argue that the existence of hydrogen atoms in the thick target region results in enhancement of HXR emission in this region. Using their ad hoc atmospheres they were able to extend the HXR source sizes to 3 arcsec on energies between 40 keV and 60 keV.

The motivation for this work is the following. Taking into account the demands on sufficient photon statistics, the typical data needed for quality RHESSI imaging are collected within several RHESSI rotations corresponding to times $\sim 10 - 10^2$ s (in Battaglia & Kontar (2011) it was 60 s). Considering the typical velocities of plasma

⋆ Corresponding author: e-mail: zdenek.moravec@ujep.cz

© 2016 WILEY-VCH Verlag GmbH & Co. KGaA, Weinheim

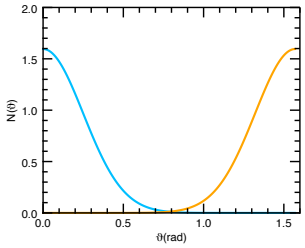

Fig. 1 The pitch-angle distributions are gaussians with the standard deviation $\sigma = 0.25$ rad. The light blue line corresponds to the strongly beamed distribution, the orange line to the pancake distribution.

flows in flare loops attained during the first several tens seconds after the onset of the impulsive phase (of orders $\sim 10 - 100$ km s^{-1}) obtained both observationally from the Doppler shift measurements in EUV/SXR (e.g. Battaglia et al. 2015; Milligan & Dennis 2009; Milligan et al. 2006) and from the hydrodynamic (HD) flare modelling (e.g. Abbett & Hawley 1999; Allred et al. 2005), substantial changes in density and column density distribution along the loop are inevitable and the time evolution of the chromospheric HXR source can arise. The resulting size and position of the HXR source detected by RHESSI will be then a result of superposition of HXR emitted in the flaring area during the whole accumulation time interval used for the image reconstruction.

In this paper we concentrate on theoretical modelling of vertical sizes and positions of chromospheric HXR sources within a singular (compact) flare loop without magnetic field convergence. The simulations are based on the CTTM (Brown 1971) in frame of the standard CSHKP flare model (see e.g. Shibata 1996). The model treats self-consistently the HD response of the chromosphere to the energy released due to the Coulomb collisions of non-thermal electrons with the chromospheric plasma on the typical timescales corresponding to RHESSI photon collection times needed for HXR image synthesis.

2 Model description

The simulations are performed using the hybrid code Flarix (Kašparová et al. 2009; Varady et al. 2014, 2010) and the VAL C atmosphere (Vernazza et al. 1981) as the initial condition. We model the atmospheric response to a single power-law electron beam generated at the apex of a single flare loop of total length $L = 15$ Mm and a constant cross-section.

The physics related to the electron beam transport, scattering and thermalisation due to Coulomb collisions (Emslie 1978) is modelled using a test-particle (TP) approach (Bai 1982) based on the Monte Carlo method. This approach, fully equivalent to the direct solution of the corresponding Fokker-Planck equation (MacKinnon & Craig 1991), provides a flexible way to model many aspects of the non-thermal electrons interactions with the ambient plasma, converging magnetic field along the loop or with additional electric fields (Varady et al. 2014). Thanks to the TP approach, the detailed distribution function of the non-thermal electrons is known at any instant time and position along the loop. This information can be used to calculate the distribution of HXR bremsstrahlung sources within the loop, their positions, sizes, spectra and directivity of the emanating HXR emission (for details see Varady et al. (2014)).

Concurrently with the transport, scattering and energy losses of the non-thermal electrons, the HD response to the released beam energy is calculated using a standard 1D HD code for low-β plasma. It models the time evolution of the plasma within a semicircular magnetic flux tube subjected to the heating by the electron beams. Hydrogen ionisation is approximated as in Brown (1973), the thermal conduction along the field lines is treated using the standard Spitzer approximation (Spitzer 1962). Total radiative losses consist of the optically thin losses from the transition region and corona (Rosner et al. 1978) and an analytic approximation of the optically thick losses from the chromosphere (Peres et al. 1982). At the loop top in the corona we assume a plane symmetry, so only one half of the loop is modelled. The boundary conditions in the corona are a solid wall for mass, a reflecting one for momentum (or velocity) and zero derivative of temperature for the heat conduction. The backscattered TPs reaching the upper boundary are reflected with a new pitch angle $\pi - \vartheta$ back into the computational domain.

The 1D gas dynamics is treated using the explicit LCPFCT solver (Oran & Boris 2000), the Crank-Nicolson algorithm for the heat transfer and the time step splitting technique to couple the individual source terms of the energy equation with the HD. More details about the code can be found in Varady et al. (2010).

3 Results

Here we discuss models of the electron beams of the power-law indices $\delta = 3, 7$, the maximum energy fluxes $F_{\rm max}$, and the low and high-energy cutoffs $E_0 = 20$ keV and $E_1 = 150$ keV, respectively. Two types of spatial initial pitch-angle distributions are considered: a strongly beamed and a pancake distribution (see Fig. 1). The energy fluxes are time dependent, linearly rising from $t = 0$ to 2.5 s to their maximum values $F_{\rm max}$ and then being kept constant during the rest of the simulation, i.e. till $t = 30$ s. The simulations showed that the energy flux $F_{\rm max} = 2 \times 10^{10}$ erg cm^{-2} s^{-1} gives too high temperatures in the corona (over 10^8 K) for the pancake distribution. The models for the pancake distribution are therefore calculated for reduced flux $F_{\rm max} = 10^{10}$ erg cm^{-2} s^{-1}, whereas the models for the beamed distribution are calculated for $F_{\rm max} = 2 \times 10^{10}$ erg cm^{-2} s^{-1}.

The time evolutions of the hydrogen number densities and energy deposits along the beam heated atmosphere are shown in Fig. 2. The patterns in the density evolution significantly vary model from model. The 'pancake' electrons

© 2016 WILEY-VCH Verlag GmbH & Co. KGaA, Weinheim

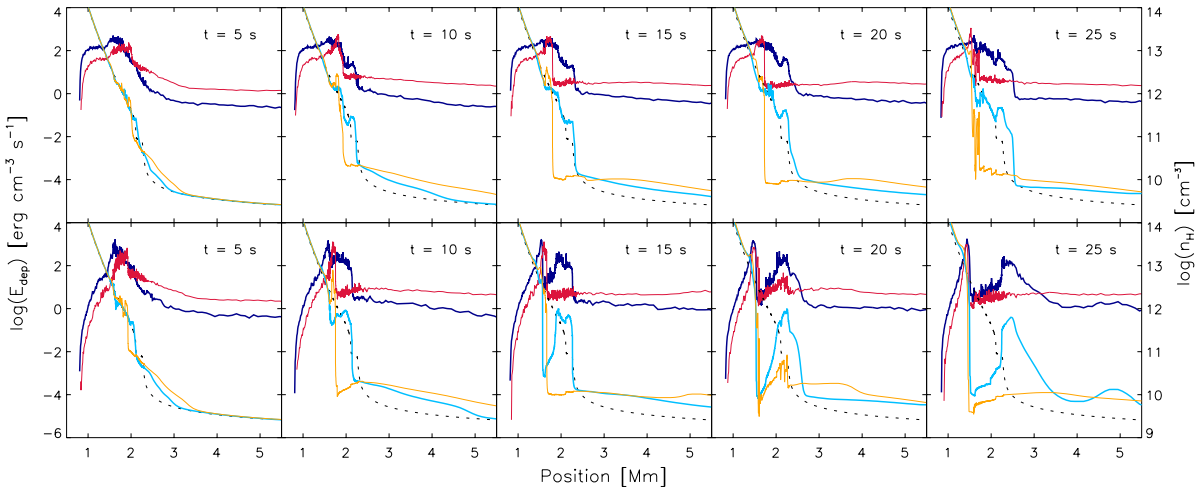

Fig. 2 Time evolution of hydrogen number densities $n_{\rm H}$ (light blue and orange lines) and energy deposits $E_{\rm dep}$ (dark blue and dark red lines) for the first 25 s. The top panels correspond to $\delta = 3$, the bottom panels to $\delta = 7$. The thick blue lines denote the beamed pitch-angle distribution and flux $F_{\rm max} = 2 \times 10^{10}$ erg cm^{-2} s^{-1}, the thin dark red and orange lines denote the pancake distribution and flux $F_{\rm max} = 10^{10}$ erg cm^{-2} s^{-1}. The dotted black lines indicates the initial $n_{\rm H}$.

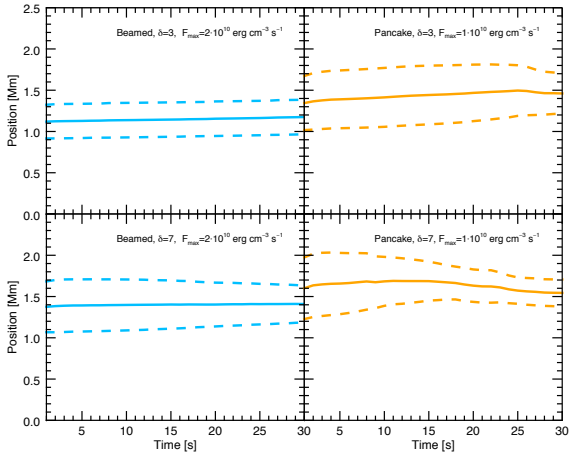
Beamed, δ=3, F_max=2·10^10 erg cm^-3 s^-1
Pancake, δ=3, F_max=1·10^10 erg cm^-3 s^-1
Beamed, δ=7, F_max=2·10^10 erg cm^-3 s^-1
Pancake, δ=7, F_max=1·10^10 erg cm^-3 s^-1
Position [Mm]
Time [s]

Fig. 3 Time evolution of HXR chromospheric footpoint source positions (solid lines) and FWHMs (dashed lines) for integrated emission in 30 – 70 keV range. The top panels correspond to $\delta = 3$, the bottom panels to $\delta = 7$. The left panels show the evolution for the beamed distribution and flux $F_{\rm max} = 2 \times 10^{10}$ (light blue), the right panels for the pancake distribution and flux $F_{\rm max} = 10^{10}$ erg cm^{-2} s^{-1} (orange).

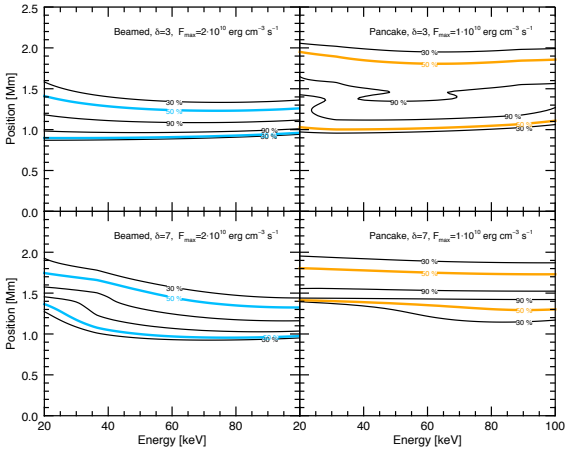
Beamed, δ=3, F_max=2·10^10 erg cm^-3 s^-1
Pancake, δ=3, F_max=1·10^10 erg cm^-3 s^-1
Beamed, δ=7, F_max=2·10^10 erg cm^-3 s^-1
Pancake, δ=7, F_max=1·10^10 erg cm^-3 s^-1
Position [Mm]
Energy [keV]

Fig. 4 Chromospheric footpoint HXR sources accumulated during the whole 30 s simulation, as a function of energy and height. The positions of individual models in the panels and color coding correspond to Fig. 3.

pass, thank to their pitch angles, much greater column densities per unit distance along the loop axis than the 'beamed' electrons. That is why they tend to deposit their energies in low density, upper layers of the atmosphere. This results in strong heating and evaporation without formation of any significant density waves. The effect is obvious for both δ, but naturally, it is more pronounced for $\delta = 7$.

The 'beamed' electrons tend to reach deeper and denser layers, where the radiative losses drain a substantial part of the deposited energy, reducing thus the energy that can be consumed on heating and evaporation. The importance of this effect increases with spectral hardness (compare the light blue lines for $n_{\rm H}$ in the top and bottom panels of Fig. 2) and results in lower plasma densities in the corona relative to the pancake distribution, at least for times ≤ 20 s. Probably because the 'beamed' energy deposits reach deeper and denser layers they tend to form strong density waves propagating with high velocities into the corona (see Fig. 2). The time evolution of the energy deposits corresponds to the density structure of the atmosphere.

To describe the characteristics of HXR emission in the modelled loop, we follow the approach of Battaglia et al. (2012) and define the position of the source as the first moment of the height profile of HXR emission and the FWHM as the second moment of that profile. Similarly, only emission above 10% of the maximum HXR is considered in or-

© 2016 WILEY-VCH Verlag GmbH & Co. KGaA, Weinheim

der to emulate the limited dynamic range of RHESSI images.

Although the density and temperature structure significantly changes (see Fig. 2), the positions and FWHMs of the HXR sources integrated in the 30 – 70 keV range change only modestly (see Fig. 3). This applies especially to the models with the beamed distribution, where the sources are static at position 1.1 Mm with FWHM 0.6 arcsec for $\delta = 3$ and 1.4 Mm with FWHM from 0.9 to 0.6 arcsec for $\delta = 7$ (see left panels in Fig. 3). For the pancake distribution and $\delta = 3$ we obtained the largest HXR source with FWHM 1.2 arcsec, placed at a constant height 1.4 Mm (see the top right panel in Fig. 3). Also the source for $\delta = 7$ (see the bottom right panel in Fig. 3) remains at constant position around 1.6 Mm, but its FWHM decreases with time from 1.1 arcsec to 0.4 arcsec. Generally, the sources corresponding to models with $\delta = 3$ are located lower than those for $\delta = 7$, and the sources for pancake distribution are located higher than those for the beamed distribution (Figs. 3, 4).

Fig. 4 shows the energy and height structure of HXR sources integrated through the duration of 30 s heating. Models of beamed pitch-angle distribution result in lower and smaller HXR sources, whereas pancake distributions correspond to larger sources located higher in the atmosphere. Both characteristics of the HXR height profile are almost independent on energy, in the 20 – 100 keV range.

4 Conclusions

Using the models of HD response to the beam heating, we studied characteristics of chromospheric flare HXR sources for the first 30 s after the start of the energy deposit for various parameters of the electron beam and two very distinct initial pitch-angle distributions.

1. In all models the assumed beam heating resulted in significant changes of density and temperature structure of the flare loop.
2. Despite the substaintial change of the atmosphere structure, the position and FWHM of the HXR sources in the 30 – 70 keV range show very weak time dependence. This is true especially for the beamed pitch-angle distribution. The model of $\delta = 7$ and pancake distribution indicates a change in FWHM with time.
3. Time averaged HXR emission through 30 s beam heating is not significantly dependent on the energy. HXR sources of the beamed distribution are smaller and located lower in comparison with models of pancake distribution.
4. HXR source characterictics are weakly related to the values of energy flux or beam power-law index, however, they show dependence on pich-angle distributions, at least for two extreme cases studied in this paper.
5. All studied models give much smaller HXR sources than observed ones, this is in agreement with previous parametric study of (Battaglia et al. 2012). The largest HXR source, 1.2 arcsec, is found for $\delta = 3$ and pancake distribution, but its location is higher than those from observations (Krucker et al. 2015) .
6. Next steps are to study influence of converging magnetic field and the effect of multi-thread structure.

Acknowledgements. We acknowledge funding from the European Community's Seventh Frame Programme (FP7/2007-2013) under grant agreement no. 606862 (F-CHROMA). D. Kramoliš and M. Varady also acknowledge the support of the UJEP Student Grant Agency. The calculations were performed on Enputron, a computer cluster at the J. E. Purkyně University, Faculty of Science.

References

Abbett, W. P. & Hawley, S. L. 1999, ApJ, 521, 906
Allred, J. C., Hawley, S. L., Abbett, W. P., & Carlsson, M. 2005, ApJ, 630, 573
Bai, T. 1982, ApJ, 259, 341
Battaglia, M., Kleint, L., Krucker, S., & Graham, D. 2015, ApJ, 813, 113
Battaglia, M. & Kontar, E. P. 2011, ApJ, 735, 42
Battaglia, M., Kontar, E. P., Fletcher, L., & MacKinnon, A. L. 2012, ApJ, 752, 4
Brown, J. C. 1971, Solar Phys., 18, 489
Brown, J. C. 1973, Solar Phys., 29, 421
Brown, J. C., Turkmani, R., Kontar, E. P., MacKinnon, A. L., & Vlahos, L. 2009, A&A, 508, 993
Emslie, A. G. 1978, ApJ, 224, 241
Fletcher, L. & Hudson, H. S. 2008, ApJ, 675, 1645
Hurford, G. J., Schmahl, E. J., Schwartz, R. A., et al. 2002, Solar Phys., 210, 61
Kašparová, J., Varady, M., Heinzel, P., Karlický, M., & Moravec, Z. 2009, A&A, 499, 923
Krucker, S., Saint-Hilaire, P., Hudson, H. S., et al. 2015, ApJ, 802, 19
Lin, R. P., Dennis, B. R., Hurford, G. J., et al. 2002, Solar Phys., 210, 3
MacKinnon, A. L. & Craig, I. J. D. 1991, A&A, 251, 693
Martínez Oliveros, J.-C., Hudson, H. S., Hurford, G. J., et al. 2012, ApJ, 753, L26
Milligan, R. O. & Dennis, B. R. 2009, ApJ, 699, 968
Milligan, R. O., Gallagher, P. T., Mathioudakis, M., et al. 2006, ApJ , 638, L117
Moravec, Z., Varady, M., Karlický, M., & Kašparová, J. 2013, Central European Astrophysical Bulletin, 37, 535
O'Flannagain, A. M., Brown, J. C., & Gallagher, P. T. 2015, ApJ, 799, 127
Oran, E. S. & Boris, J. P. 2000, Numerical Simulation of Reactive Flow (Cambridge, UK: Cambridge University Press), p. 258
Peres, G., Serio, S., Vaiana, G. S., & Rosner, R. 1982, ApJ, 252, 791
Rosner, R., Tucker, W. H., & Vaiana, G. S. 1978, ApJ, 220, 643
Shibata, K. 1996, Advances in Space Research, 17, 9
Spitzer, L. 1962, Physics of Fully Ionized Gases (New York, USA: Interscience), p. 120–147
Turkmani, R., Cargill, P. J., Galsgaard, K., Vlahos, L., & Isliker, H. 2006, A&A, 449, 749
Varady, M., Karlický, M., Moravec, Z., & Kašparová, J. 2014, A&A, 563, A51
Varady, M., Kašparová, J., Moravec, Z., Heinzel, P., & Karlický, M. 2010, IEEE Transactions on Plasma Science, 38, 2249

© 2016 WILEY-VCH Verlag GmbH & Co. KGaA, Weinheim

Varady, M., Moravec, Z., Karlický, M., & Kašparová, J. 2013, Journal of Physics: Conference Series, 440, 012013
Vernazza, J. E., Avrett, E. H., & Loeser, R. 1981, ApJS , 45, 635

© 2016 WILEY-VCH Verlag GmbH & Co. KGaA, Weinheim